



# Serial Flaring in an Active Region: Exploring Why Only One Flare Is Eruptive

Magnus M. Woods<sup>1,2,3,4</sup> , Satoshi Inoue<sup>2</sup> , Louise K. Harra<sup>1</sup> , Sarah A. Matthews<sup>1</sup> , and Kanya Kusano<sup>2</sup> <sup>1</sup>Mullard Space Science Laboratory, University College London, Dorking, Surrey, RH5 6NT, UK; [woods@baeri.org](mailto:woods@baeri.org)<sup>2</sup>Institute for Space-Earth Environmental Research (ISEE)/Nagoya University Furo-cho, Nagoya, Aichi 464-8601, Japan<sup>3</sup>Bay Area Environmental Research Institute (BAERI), P.O. Box 25 Moffett Field, CA 94035, USA<sup>4</sup>Lockheed Martin Solar and Astrophysics Lab, Palo Alto, CA 94304, USA

Received 2019 July 16; revised 2020 January 3; accepted 2020 January 13; published 2020 February 14

## Abstract

Over a four hour period between 2014 June 12–13 a series of three flares were observed within AR 12087. This sequence of flares started with a non-eruptive M-class flare, followed by a non-eruptive C-class flare, and finally ended with a second C-class flare that had an associated filament eruption. In this paper we combine spectroscopic analysis of *Interface Region Imaging Spectrometer* observations of the Si IV line during the three flares along with a series of nonlinear force-free field (NLFFF) extrapolations in order to investigate the conditions that lead the final flare to be eruptive. From this analysis it is found to be unlikely that the eruption was triggered by either kink instability or by tether-cutting reconnection, allowing the flux rope to rise into a region where it would be susceptible to the torus instability. The NLFFF modeling does, however, suggest that the overlying magnetic field has a fan-spine topology, raising the possibility that breakout reconnection occurring during the first two flares weakened the overlying field, allowing the flux rope to erupt in the subsequent third flare.

*Unified Astronomy Thesaurus concepts:* [Solar flare spectra \(1982\)](#); [Solar physics \(1476\)](#); [Solar active regions \(1974\)](#); [Solar activity \(1475\)](#); [Solar active region magnetic fields \(1975\)](#); [Solar active region filaments \(1977\)](#); [Solar flares \(1496\)](#)

## 1. Introduction

Several decades of research both observational and theoretical have revealed a number of different processes and mechanisms through which solar flares and their associated eruptions can be triggered. These mechanisms can be broadly split into two categories: reconnection-driven processes, such as tether-cutting reconnection (Moore & Labonte 1980; Moore et al. 2001) and magnetic breakout (Antiochos et al. 1999); and ideal MHD instabilities such as the torus instability (Bateman 1978; Kliem & Török 2006), kink instability (Török & Kliem 2005), or double arc instability (DAI; Ishiguro & Kusano 2017).

While many studies focus on one flare or several flares from different active regions, it is important to note that within individual active regions flaring is not usually isolated to one event. Sequential flaring can provide an excellent test of flare-trigger models allowing us to investigate whether all flares in the sequence are triggered by the same process, and, whether there are consistent pre-flare signatures. Examples of this kind of study can be found in Nitta & Hudson (2001), Romano et al. (2015), and Polito et al. (2017). This paper will investigate one such sequence of flares.

Late on 2014 June 12, and extending into early 2014 June 13, a series of three flares were observed from active region (AR) 12087. The sequence contained two non-eruptive flares, of M and C-class, followed by an eruptive C 8.0 flare. The first flare in the sequence, the M 1.0 flare, is the subject of papers by Sadykov et al. (2016) and Sharykin et al. (2017). Both papers make use of New Solar Telescope data, with Sadykov et al. (2016) also using data from the *Interface Region Imaging*

*Spectrometer (IRIS; DePontieu et al. 2014)*, to investigate chromospheric evaporation, and Sharykin et al. (2017) using data in combination with nonlinear force-free field (NLFFF) modeling to investigate energy deposition at the polarity inversion line during the flare. Kumar et al. (2015) also investigate two of the flares in the sequence, using their observations to reach the conclusion that flux cancellation in the AR resulted in the build up of a twisted magnetic flux rope, which subsequently erupted.

In this paper we also use *IRIS* spectroscopic data, in combination with a series of NLFFF extrapolations to investigate the series of flares between 2014 June 12–13. We seek to determine why only the final flare in this sequence was eruptive despite it not being the largest *GOES* classification in the sequence.

## 2. Observations and Method

The data used in the analysis presented in this paper were drawn from several sources. *IRIS* was observing AR 12087 for several hours as part of a long-duration flare-watch observing program. *IRIS* was observing from 2014 June 12 18:44 UT to 2014 June 13 03:53 UT, with a raster field of view of  $14'' \times 62''$  and a cadence of 21 s. *IRIS*'s slit-jaw imager (SJI) was also observing in the 1330 Å and 2796 Å passbands.

The *Solar Dynamics Observatory (SDO; Pesnell et al. 2012)*, which carries the Helioseismic and Magnetic Imager (HMI; Scherrer et al. 2012), provides the observations of the photospheric magnetic field utilized in this paper. Vector magnetograms prepared in the Spaceweather HMI Active Region Patch (SHARP) format (Bobra et al. 2014), were used to calculate NLFFF extrapolations using the magnetohydrodynamic relaxation method presented in Inoue et al. (2014) and Inoue (2016). This method uses observed photospheric magnetic fields as lower boundary conditions to find and constrain suitable force-free fields. Initially a potential field is

extrapolated from the  $B_z$  component of the photospheric field, which is determined uniquely (Sakurai 1982). The horizontal magnetic fields ( $B_{\text{pot},x}$ ,  $B_{\text{pot},y}$ ) on the lower boundary, which are potential components extrapolated from  $B_z$ , are then gradually changed to match the observed horizontal fields, ( $B_{\text{obs},x}$ ,  $B_{\text{obs},y}$ ). While this process occurs on the bottom boundary, the magnetic fields are fixed to the potential field at the other boundaries. We also solve the following equations inside of a numerical box until the solution converges to a quasi-static state,

$$\rho = |\mathbf{B}|, \quad (1)$$

$$\frac{\partial \mathbf{v}}{\partial t} = -(\mathbf{v} \cdot \nabla) \mathbf{v} + \frac{1}{\rho} \mathbf{J} \times \mathbf{B} + \nu \nabla^2 \mathbf{v}, \quad (2)$$

$$\frac{\partial \mathbf{B}}{\partial t} = \nabla \times (\mathbf{v} \times \mathbf{B} - \eta \mathbf{J}) - \nabla \phi, \quad (3)$$

$$\mathbf{J} = \nabla \times \mathbf{B}, \quad (4)$$

$$\frac{\partial \phi}{\partial t} + c_h^2 \nabla \cdot \mathbf{B} = -\frac{c_h^2}{c_p^2} \phi, \quad (5)$$

where  $\rho$  is pseudo plasma density,  $\mathbf{B}$  the magnetic flux density,  $\mathbf{v}$  the velocity,  $\mathbf{J}$  the electric current density, and  $\phi$  the convenient potential to reduce errors derived from  $\nabla \cdot \mathbf{B}$  (Dedner et al. 2002).  $\nu$  is a viscosity term fixed at  $1.0 \times 10^{-3}$ , and the coefficients  $c_h^2$ ,  $c_p^2$  in Equation (5) are also fixed with constant values, 0.04 and 0.1, respectively. The resistivity is given as  $\eta = \eta_0 + \eta_1 |\mathbf{J} \times \mathbf{B}| |\mathbf{v}| / |\mathbf{B}|$ , where  $\eta_0 = 5.0 \times 10^{-5}$  and  $\eta_1 = 1.0 \times 10^{-3}$  in non-dimensional units. The second term is introduced to accelerate the relaxation to the force-free field, particularly in weak field regions. The details of this NLFFF extrapolation method are further described in Inoue et al. (2014) and Inoue (2016). The extrapolations presented in this paper were created in a numerical box covering an area of  $216 \times 216 \times 216$  (Mm<sup>3</sup>), which is given as  $1.0 \times 1.0 \times 1.0$  in non-dimensional units. The region is divided into  $300 \times 300 \times 300$  grid cells, which is a result of  $2 \times 2$  binning of the original SHARPS vector magnetic field.

Data from the Atmospheric Imaging Assembly (AIA; Lemen et al. 2012), also on board *SDO*, are used to provide context images for the observations in various wavelengths, additional lightcurves, and to provide a suitable reference for co-alignment between the different instruments. *Reuven Ramaty High Energy Spectroscopic Imager (RHESSI; Lin et al. 2002)* observations were also utilized in this work. Images in the 12–25 keV and 25–50 keV energy ranges were reconstructed using the CLEAN algorithm.

### 3. Results

Between 21:00 UT on 2014 June 12 and 01:30 UT on 2014 June 13, AR 12087, situated in the south eastern quadrant of the solar disk, produced three flares. These flares were as follows: an M1 flare peaking at 21:18 UT, a flare peaking at 22:51 UT, and a C8 flare peaking at +1 00:36 UT. Panel (a) of Figure 1 shows the *GOES* soft X-ray lightcurve of solar activity between 20:30 UT on 2014 June 12 and 01:30 UT on 2014 June 13. It is important to note that while three flares are present in this lightcurve, the middle flare does not correspond to the second flare produced by AR 12087, but in fact corresponds to an M3.1 flare produced by AR 12085, situated

in the lower western quadrant of the solar disk. Panel (b) shows a lightcurve of only AR 12087 produced from AIA 94 Å passband data. In this we clearly see the three flares produced by AR 12087 during this time period, with the 22:51 flare unobscured by the M3.1 flare as in the *GOES* lightcurve. From this *SDO* lightcurve, this second flare is therefore estimated to be of C-class. While serial flaring is of interest on its own, the sequence of flares exhibited in AR 12087 also has only one associated eruption. While one may expect the eruption to be associated with the largest flare (Harra et al. 2016 studied 42 X-class flares, finding only 9 to have no associated eruption), we find that in this case the eruption occurs during the final C8 flare at +1 00:36 UT.

Figure 2 shows AR 12087 as observed by the *IRIS* SJI 1330 Å at four times; 21:06 UT (flare 1, panel (a)), 22:41 UT (flare 2, panel (b)), +1 00:34 UT (flare 3 and eruption, panel (c)), and +1 00:43 UT (flare 3, panel (d)). Panels (a), (b), and (d), show the morphology of the M1, C, and C8 flares respectively, while panel (c) shows the structure of the eruption during the early stages of the C8 flare. The arrow in this panel shows the direction of the eruption toward the southeast. Figure 2 shows clear morphological similarities between all three flares. All exhibit semi-circular flare ribbons. Additionally, the earliest signs of flaring appear to begin from the same region in all of the flares (marked by the arrow in panel (a) of Figure 2). The positions of the initial ribbon brightenings of each flare in AIA 1600 Å are shown in Figure 3. These initial brightenings were defined as being 40 standard deviations above the quiet Sun background. We can see that the initial brightenings are all located in the same region that was also identified from the *IRIS* SJI data in Figure 2.

One clear difference between the flares, along with *GOES* class, is their eruptive nature. As we have already noted, flares 1 and 2, M1 and C-class, respectively, are non-eruptive flares, while flare 3, C8 class, is eruptive. Kumar et al. (2015) provide an overview of this AR in an effort to investigate the subsequent eruption. However, their work does not investigate the full time sequence between the flares, which excludes the second flare. This work aims to revisit this active region and attempt to determine why only the C8 flare was eruptive, by examining the evolution including the second flare. This work is carried out using a combination of spectroscopic observations and NLFFF modeling, and also seeks to determine whether the pre-flare signatures the authors have previously observed in Woods et al. (2017, 2018) are also seen to occur prior to the three flares in this sequence.

#### 3.1. Characteristics of the Three Flares

As we noted from Figure 2, the three flares in the sequence are somewhat homologous in terms of ribbon morphology, with all exhibiting semi-circular flare ribbons. To investigate the reasons why only the third flare in the sequence was eruptive, several observational parameters were studied.

##### 3.1.1. Evolution of Lightcurves

Several regions for further study were selected and lightcurves were produced to study the flare evolution. These lightcurves were produced from AIA 193 Å observations. Figure 4(a) shows the locations of the regions in which the three largest field-of-view lightcurves were produced overlaid onto HMI line-of-sight (LOS) magnetogram and AIA 193 Å

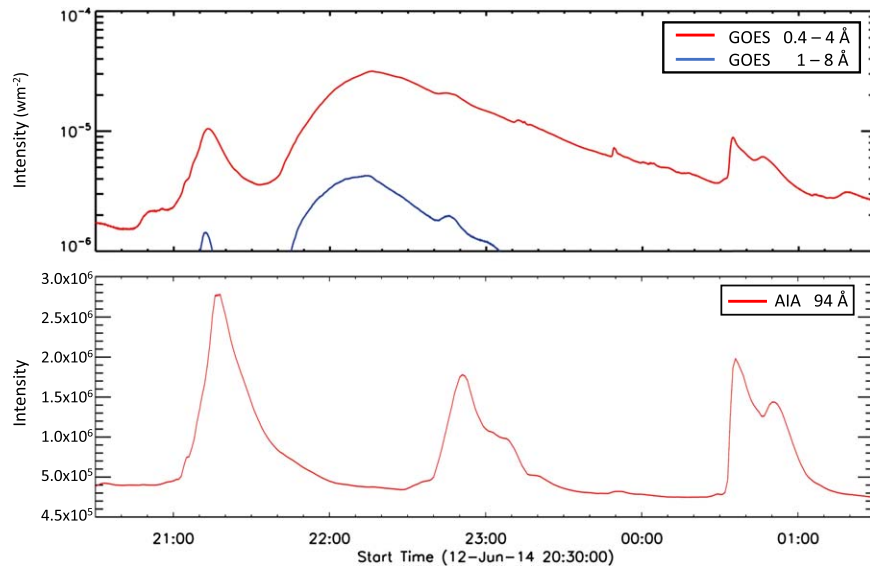


**Figure 1.** Panel (a) shows the *GOES* lightcurve of the soft X-ray flux of the whole solar disk, from 2014 June 12 20:30 UT. The red and blue curves correspond to the 0.4–4 Å and 1–8 Å channels respectively. The first and last flares seen in this lightcurve occur in AR 12087, while the middle flare is an M 3.1 flare produced by AR 12085. This M 3.1 flare obscures the second flare in the sequence produced by AR 12087. Panel (b) shows the AIA 94 Å lightcurve for AR 12087. We can clearly see that in the *GOES* lightcurve (panel (a)) the 22:51 UT C-flare is obscured by an M3.1 flare occurring in AR 12085.

images. These three regions correspond to AR 12087, the region which produced the series of flares, its neighboring active region AR 12092 situated to its east at the same latitude, and finally the region, denoted LR, contains the footpoints of a system of overlying magnetic field, which appears to connect to AR 12087.

The lower panels of Figure 4 show the AIA 193 Å lightcurves for the three selected regions. The overlaid dotted–dashed lines correspond to the start and end times for the three flares as determined from the AIA 94 Å lightcurves. These times were identified using definitions chosen to match the criteria used by the *GOES* flare list. Flare start was defined as the time when intensity had increased constantly over a four minute period and the final intensity value in the four minute period was 1.4 times the intensity of the first. Flare end time was defined as the time when post-flare intensity reached half the flare maximum. The lightcurve for AR 12087 is shown in panel (b), clearly showing the sequence of three flares. The three flare lightcurves show different forms: flare 1 exhibits a double peak, flare 2 has a more gradual appearance, while flare 3 shows a far more impulsive profile, with a gradual decay post eruption. Panel (c) shows the lightcurve for the region LR. Prior to and during flare 1, we clearly see an intensity enhancement within this region. A very slow increase in intensity is observed to begin during flare 2, while there is a decrease in intensity during flare 3. The final panel (d) details the evolution of intensity in AR 12092. From the start of the lightcurve at 19:00 UT until +1 00:00 UT there is little correlation between the activity within AR 12092 and AR 12087. At +1 00:15 UT a flare is observed to occur in AR 12092. This is then followed by a second flare peak, with an associated failed eruption, which is coincident in time with the eruptive C 8 flare in AR 12087. The fact that there are two flares and eruptions occurring simultaneously in separate active regions may suggest the existence of overlying magnetic fields linking the two regions that may play a role in the triggering of the eruptions. This will be discussed further in Section 4.

### 3.1.2. Evolution of Magnetic Flux

Figure 5 shows the evolution of the positive and negative flux of the  $B_r$  component of the vector magnetic field as measured by HMI, AIA 193 Å intensity, and *IRIS* SJI 1330 Å intensity (panels (b), (c) and (d), respectively) between 19:00 UT and +1 01:30 UT. The shaded regions in panel (b) and the dotted–dashed lines present in panels (c) and (d) highlight the start and end times of each of the flares as determined from the AIA 94 Å data, as described earlier. Panel (a) shows the central portion of the active region with the region over which the lightcurves are calculated marked by the overlaid box. Panels (c) and (d) show clear intensity increases during each of the flares. There are differences in the profiles of these increases, most notably during flare 1 where the *IRIS* 1330 Å emission peaks several minutes prior to the AIA. These difference can likely be accounted by the difference in level of the atmosphere being observed with the AIA 193 Å data detailing the coronal response, while the *IRIS* 1330 Å lightcurve shows the transition region/chromospheric response to the flare. Panel (b) shows the evolution of the absolute value of positive and negative magnetic flux of the  $B_r$  component of the vector magnetic field in cylindrical equal area (CEA) coordinates. We can see that over the course of the lightcurve both positive and absolute value of negative flux show a decreasing trend between 19:00 UT and +1 01:46 UT. Aside for this general trend in decreasing flux over the course of the observation period, there are sharp drops in both positive and negative flux seen prior to and during both flares 1 and 2. These coincident decreases in flux are indicative of flux cancellation occurring in the lead up to the two non-eruptive flares. These two flux cancellation instances are observed up to 20 minutes prior to the onset of flares 1 and 2. In the case of flare 3, the eruptive C 8 flare, evidence of flux cancellation prior to flaring is not as clear. We can see from Figure 5 that there is a clear decrease in positive flux observed before, during, and after flare 3. The evolution of negative flux in this time period differs, with an initial, but smaller, decrease prior to flaring, which is

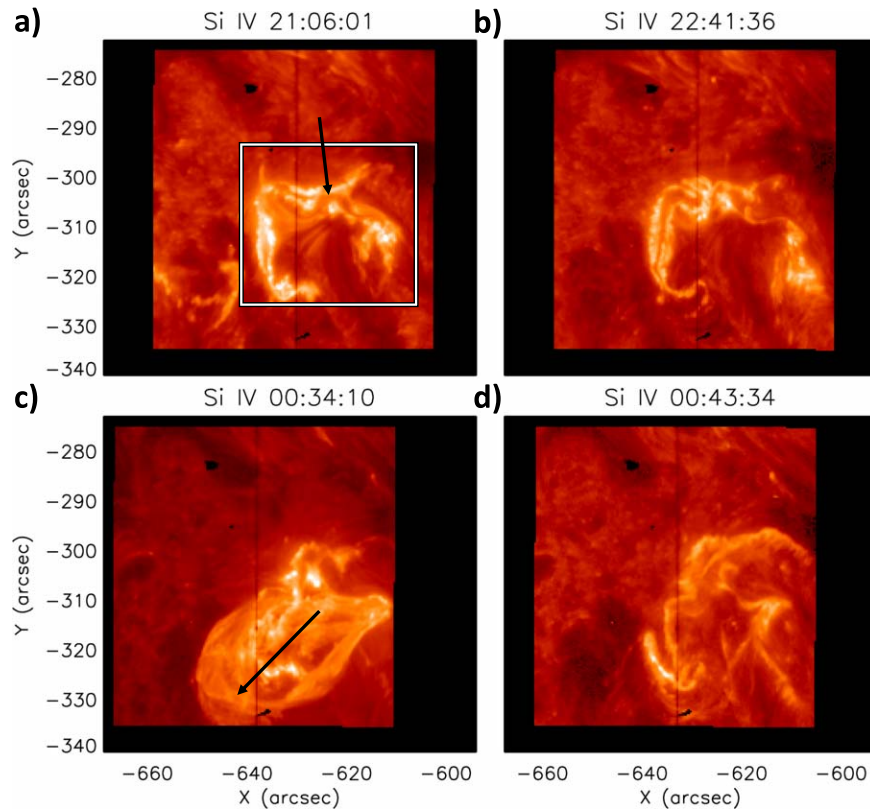


**Figure 2.** *IRIS* SII 1330 Å images of the three flares and the eruption. Panel (a) shows the M 1 flare at 21:06 UT. The region in which the earliest signs of flaring are observed is marked with the black arrow. The box highlights the field of view shown in Figure 3. Panel (b) shows the C-flare at 22:41 UT. Panel (c) clearly shows the eruption during the c-flare at 00:34 UT, with the black arrow showing the direction of the eruption. Panel (d) shows the post-eruption ribbon structure at 00:43 UT.

then followed by a similarly sized increase in negative flux, which returns to its pre-decrease value.

### 3.1.3. Evolution of the Recurring Bright Point Region

Within the central portion of AR 12087 there is also a recurring bright point, the location of which is marked by the black arrows in Figures 2(a) and 6(a). The overlaid boxes in Figure 3 also highlight this region. This bright point is seen to occur prior to and during all three flares, and appears to be the region showing the earliest response to the flaring.

Figure 6(a) shows *IRIS* Si IV intensity contours (black) overlaid onto the AIA 193 Å observations during flare 1. The black box highlights the field of view of the *IRIS* raster during the observations. While the *IRIS* raster covers the majority of the flare ribbons, it unfortunately only extends to the eastward edge of the recurring bright point region. We can see the region of saturation (indicated by the arrow), which is the region of first response to flaring as well as the location of the recurring bright point region. Panel (b) of Figure 6 shows the full *IRIS* Si IV raster data for intensity during flare 1. The bright region marked by the box on the westward edge of the *IRIS* field of view corresponds to the aforementioned AIA bright point region as it extends into the raster field of view. Figure 6(c) shows the evolution of *IRIS* Si IV raster intensity. This lightcurve is made from the data within the small region marked by the box in Figure 6(b). We can see that this lightcurve clearly shows the three flares. However, the profiles of the intensity enhancements related to each flare are clearly different to those of the AIA 193 Å. Additionally, prior to flares 1, 2, and the eruptive flare 3, intensity enhancements can be

seen. These enhancements start  $\sim 10$  minutes prior to flare 1,  $\sim 18$  minutes prior to flare 2, and  $\sim 23$  minutes prior to flare 3. Panel (d) shows the evolution of the spectral line width with time on a velocity scale. The profiles shown are the total of all emission within the box marked in Figure 6(b). Each individual sub-panel of Figure 6(d) corresponds to 2 hr of observation around the peak of each of the three flares. We can see the three flares clearly in all three time profiles, which are observed as the darkest regions in the profiles as a reversed color table is used. The start and end times of the three flares are also marked by the horizontal dotted lines in the time profiles. Additionally, overplotted in blue are representative pre-flare spectra for each flare. From the three time profiles we can clearly see that, as we noted from the lightcurve above, there is evidence of emission within this region prior to the onset of flaring as defined from the AIA 94 Å data. This is most notable for flare 2 and flare 3, where for several minutes ( $>15$  minutes) prior to flare start we see intensity enhancements. These enhancements in intensity are accompanied by redshifts in the case of flare 2, and both red and blueshifts in the case of flare 3. For flares 1 and 2 in the minutes immediately prior to flaring, strong intensity enhancements can be seen as well as increases in the redshifted emission observed. These redshifted spectra show emission up to  $\sim$ hundreds of  $\text{km s}^{-1}$ . These redshifts are clearly seen in the representative spectra. In the case of flare 3, which was the eruptive flare, we see that the intensity pre-flare enhancements are stronger for longer, on the order of  $\sim 8$  minutes. These intensity enhancements are also accompanied by both red and blueshifted emission, again extending to  $\sim$ hundreds of  $\text{km s}^{-1}$ . This is clearly shown in the example line profile overplotted in blue, where the simultaneously observed red/blueshifts are

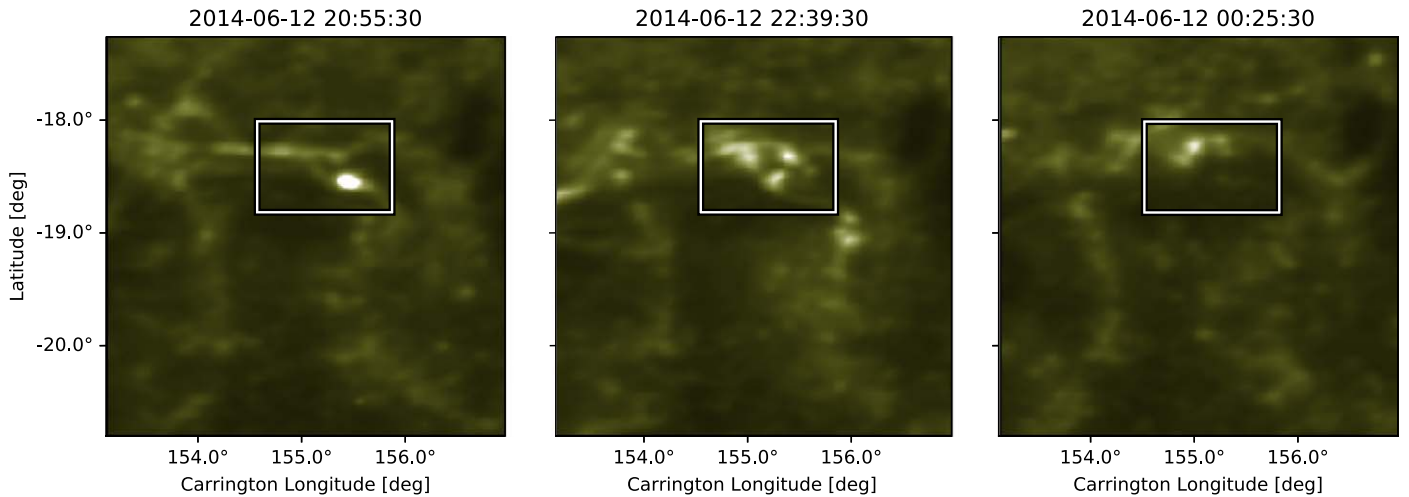


**Figure 3.** AIA 1600 Å images of the first flare ribbon brightenings prior to each of the three flares under study. Panels (a), (b), and (c) show the initial ribbon brightenings of flares 1, 2, and 3, respectively. The plotted data are shown in CEA projection. The overlapped boxes in the three panels highlight the region in which the recurring brightpoints are observed.

seen to originate in the wide Lorentzian-like profile of the line. The non-thermal velocity of spectra within this region was also calculated. During non-flaring times the median non-thermal velocity exhibited values of  $\sim 20 \text{ km s}^{-1}$  rising to  $\sim 40 \text{ km s}^{-1}$  during non-flaring times. Individual maximum values of non-thermal velocity within the region regularly exceed  $70 \text{ km s}^{-1}$ , occasionally reaching values of over  $100 \text{ km s}^{-1}$ .

#### 3.1.4. Evolution of Flare Ribbon Area

Recent work by Toriumi et al. (2017) examined several properties of solar flares and the active regions that produced them, in order to investigate their relationship between the eruptive nature of the flares. The ratio of two such properties, flare ribbon area ( $S_{\text{ribbon}}$ ) and sunspot area ( $S_{\text{spot}}$ ), were found to be an indicator of whether a flare was eruptive or not. In this context  $S_{\text{ribbon}}$  is the cumulative area of the flare ribbons, and  $S_{\text{spot}}$  is the area of the sunspots within the active region in which the flare occurs. To further investigate the differences between the three flares in AR 12087, the  $S_{\text{ribbon}}/S_{\text{spot}}$  was calculated for each flare, following the method of Toriumi et al. (2017). In this method, a flare ribbon is defined as being any brightening within the active region that has intensity greater than  $40\sigma$  of the mean quiet Sun intensity in the AIA 1600 Å passband. The total ribbon area,  $S_{\text{ribbon}}$  is determined as being the sum of all regions that meet the stated intensity threshold in all non-saturated AIA 1600 Å exposures from 20 minutes prior to flaring until flare end. HMI continuum observations were used to determine  $S_{\text{spot}}$ , where, in the same field of view as was used to identify the flare ribbons, the sunspot was defined as any region with intensity less than 85% of the mean quiet-Sun intensity. Figure 7 shows the distribution of  $S_{\text{ribbon}}$  and  $S_{\text{spot}}$  for all three of the flares.

Table 1 shows the values of  $S_{\text{ribbon}}$ ,  $S_{\text{spot}}$ , and their ratio for the three flares under study. What we find is that  $S_{\text{ribbon}}/S_{\text{spot}}$  is smallest for the eruptive flare, counter to the conclusions of Toriumi et al. (2017) who found that in general  $S_{\text{ribbon}}/S_{\text{spot}}$  is larger for eruptive flares. However, it is important to note that the two distributions of  $S_{\text{ribbon}}/S_{\text{spot}}$ , shown in Figure 4 of Toriumi et al. (2017), for eruptive and non-eruptive flares, overlap significantly. In the case of the values we see for the three flares studied in this work, the values of  $S_{\text{ribbon}}/S_{\text{spot}}$  all

fall within the distributions found by Toriumi et al. (2017) for their eruptive class.

#### 3.1.5. RHESSI Observations

We have investigated the response of several regions of the solar atmosphere to three flares, through photospheric LOS magnetograms, to transition region *IRIS* Si IV observations and the coronal response as seen through the AIA 193 Å observations. During these three flares *RHESSI* was operational, therefore allowing the X-ray emission during these flare to be investigated. Figure 8 shows the *RHESSI* 12–25 keV (red contours) and 25–50 keV (blue contours) emissions overlaid onto AIA 1600 Å observations. The *RHESSI* images were reconstructed using the CLEAN algorithm. Panel (a) shows the situation at 21:11 UT, during the M 1 flare. In the AIA 1600 Å we can clearly see the flare ribbons. The *RHESSI* observations show one unresolved source in the 12–25 keV range that is coincident with the flare ribbons. Panel (b) shows the same field of view at 22:43 UT. As before we can discern the flare ribbons from the C-flare. During this flare we observe two resolved X-ray sources in the 12–25 keV energy range. During the C 8 flare and the eruption, panel (c) at +1 00:33 UT, we again see one unresolved source in the 12–25 keV energy band, which is again coincident with the flare ribbons. However, a clear difference between the eruptive C 8 flare and the previous flares is the presence of higher energy X-rays in the form of two resolved sources in the 25–50 keV energy band. This emission can be seen to once again correspond to the location of the flare ribbons.

Temmer et al. (2010) note somewhat similar behavior in a study looking at the relationship between coronal mass ejection (CME) and particle acceleration. In one of the eruptive events studied they observed a short-lived single hard X-ray (HXR) burst of high flux density with a very hard (i.e., large numbers of high energy electrons) HXR spectrum, but which had a relatively low total electron energy and *GOES* classification. They explain this behavior as the result of feedback between the CME acceleration and flare reconnection (Vršnak 2008)—increasing flare reconnection rate boosts CME acceleration and vice versa, enhanced acceleration provides more efficient

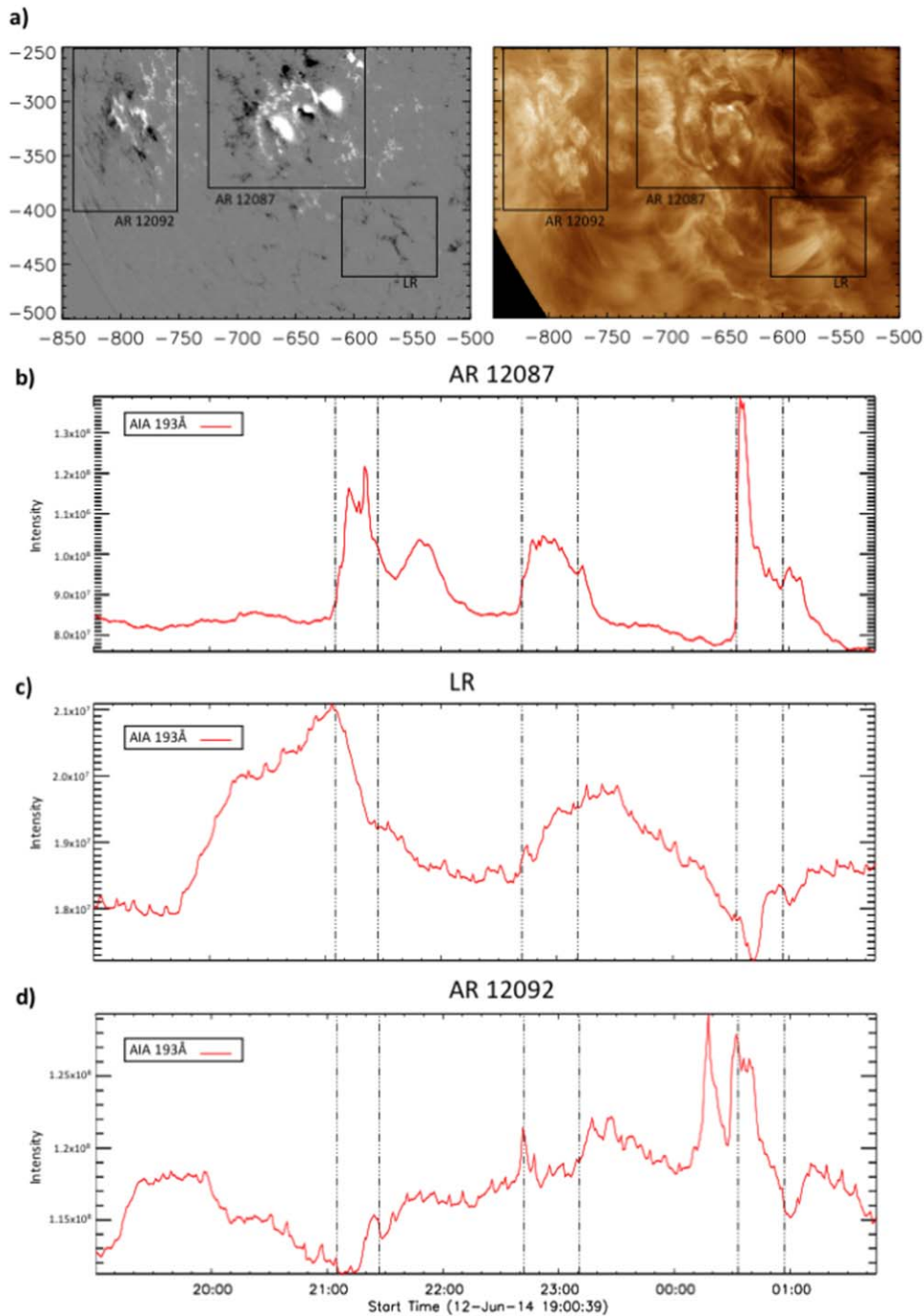


**Figure 4.** Panel (a) shows the fields of view in which lightcurves are calculated over shown in HMI LOS magnetogram and AIA 193 Å; AR 12087 that produced the three observed flares; AR 12092 that is the AR neighboring AR 12087; and LR, which corresponds to a region to the south of AR 12087 that is magnetically linked. Panels (b)–(d) show the resultant lightcurves respectively. The dotted–dashed lines overlaid mark the start and end times of each of the flares in the sequence.

reconnection, leading to more efficient particle acceleration. Such behavior would be consistent with our observations.

### 3.2. Magnetic Field Extrapolations

To investigate the 3D magnetic structure of AR 12087 we produced four NLFFF extrapolations. The timings of these extrapolations were chosen to be pre and post each flare in the sequence, i.e., 20:48 UT, 22:24 UT, +1 00:24 UT, and +1 01:36 UT. Figure 9 shows the results of these four extrapolations. The red field lines are plotted emanating from within a small box at the eastern footpoints of the plotted field lines.

This region lies on the PIL and was selected for plotting the field lines due to the high twist values exhibited there. The blue field lines are plotted from another box defined to the east of this high twist region, within the region of negative magnetic flux. The blue field lines clearly show a loop system that extends from the central portion of the active region to a positive eastward sunspot.

Over the course of the series of extrapolations from 20:48 UT until +1 00:24 UT, we see what appears to be the formation of an extended twisted tail-like feature. In the post-eruption extrapolation from +1 01:36 UT the tail-like feature

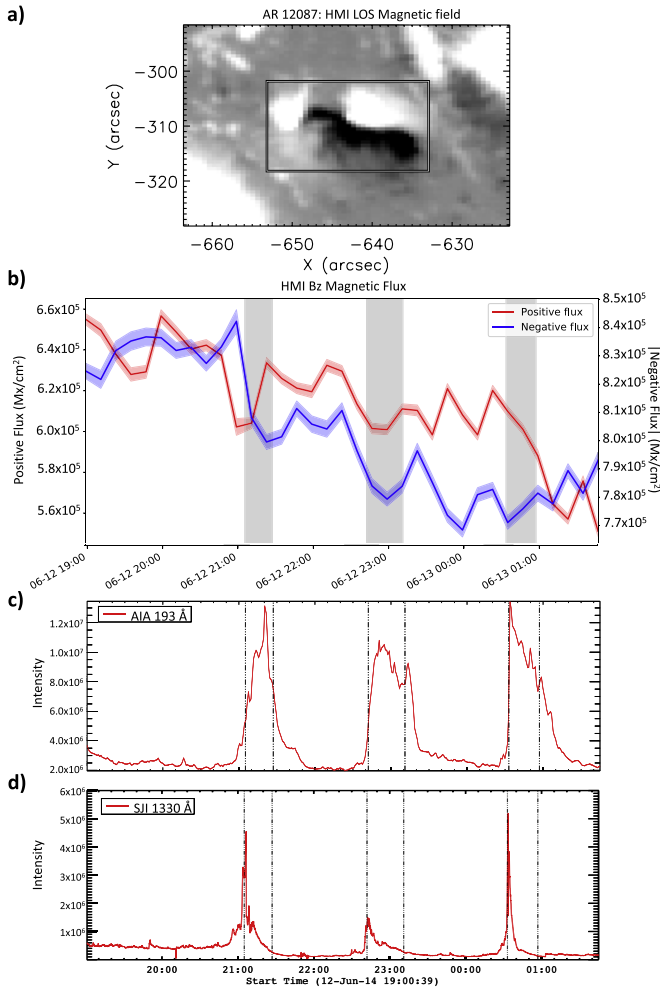


**Figure 5.** Panel (a) shows the central portion of AR 12087, with the overlaid box marking the region in which the magnetic flux and lightcurves were calculated. Panel (b) shows the evolution of positive and negative magnetic flux between 19:00 UT and +1 01:30 UT. Panel (c) shows the AIA 193 Å lightcurve, and panel (d) shows the IRIS SJI 1330 Å for the same time range and region. The overlaid shaded regions and dotted-dashed lines in each lightcurve represent the start and end times of each flare in the series.

appears to have decreased in length. Panel (e) of Figure 9 shows a comparison between the extrapolated field lines and loops seen in the 131 Å channel. The left hand image shows the field lines overlaid onto the 131 Å data while the right hand image shows the same field of view and field lines overlaid onto the magnetic field observations. As we can see the blue extrapolated field lines match the location of the extended loop we see in the 131 Å image. Thus we can deduce that our extrapolation has reproduced the structure of the observed loops and hence, the magnetic structure of the active region with some accuracy. Our NLFFF extrapolation code (Inoue et al. 2014; Inoue 2016) is currently unable to numerically quantify the uncertainties of the extrapolation results, and therefore we are likewise unable to provide numerical values for the uncertainties for the quantities derived (e.g., twist and decay index) from them in the following section. However, as the extrapolation is clearly reproducing the morphological structure of the active region, we are satisfied that the derived quantities are similarly accurate. It should also be noted that the extrapolation uses SHARPS vector magnetic field data as its lower boundary condition. These data are projected into

CEA coordinates. For our comparison we have re-projected the AIA 131 Å to the cea coordinate system to allow the direct comparison of the two data sets.

### 3.2.1. Twist Evolution

As we have seen morphological changes in the field lines, the evolution of magnetic twist derived from the extrapolations are then investigated to determine if the morphological changes are accompanied by large increases or decreases in twist. We define twist( $T_w$ ) as follows

$$T_w = \frac{1}{4\pi} \int \frac{\nabla \times \mathbf{B} \cdot \mathbf{B}}{|\mathbf{B}|^2} dl, \quad (6)$$

where  $dl$  is a line element of a field line. Figure 10(a) shows the  $B_z$  map and twist map of AR 12087. Marked by the overlaid boxes are the two regions in which the evolution of twist is investigated. Region 1 corresponds to the central portion of the AR, while Region 2 encompasses an area of higher twist, which appears to be co-spatial with the tail-like structure that develops in the later extrapolations. Histograms for these regions are shown in panels (c) and (d), respectively. Additionally, the twist within the ribbon areas for each flare, see Figure 7, were calculated and are shown in panel (b). In these figures for each flare, respectively, pre-flare twist is shown in blue and post-flare twist is shown in red. The evolution of twist within the flare ribbon areas shown in panel (b) in general shows little clear evolution before pre and post flaring. Over the course of flare 1, between 20:48 UT and 22:24 UT, the highest twist values increase slightly, while the number of the lowest twist values increases also. Over flare 2, between 22:24 UT and +1 00:24 UT the highest twists values are seen to decrease in count slightly. Over the course of the eruptive flare 3, +1 00:24 to +1 01:34 UT, a small increase in the highest twist values is shown, along with an increase in the number of lower twist values.

Panels (c) and (d) of Figure 10 show the change in twist between each flare for regions 1 and 2 respectively.

For region 1 we can see that during the first flare there is little change in twist. Twist between 22:24 UT and +1 00:24 UT shows little change beyond an increase in the peak of the distribution twist value. Finally between the +00:24 UT and +1 01:36 UT there is again little change in the twist value, besides the peak of the distribution shifting slightly from  $T_w \sim 0.4$  to  $T_w \sim 0.3$ . In the case of region 2 (Figure 10(c)), between all the flares we note that the general profile of the twist distribution changes very little over the course of the three flares and the eruption. However, in this region there is a small secondary peak at high twist values. This peak is present at 21:00 UT at  $T_w = 1.3$ , but is not present in the 22:24 UT histogram. This same peak appears once again in the +1 00:24 UT extrapolation, peaking at  $T_w = 1.3$ . Once more this peak is found to disappear from the histogram between +1 00:24 UT and +1 01:36 UT.

### 3.2.2. Decay Index

From the extrapolations we can also determine the distribution of decay index within the active region. This was done to investigate the stability of the structures that we have identified in the extrapolations to the torus instability. The dimensionless

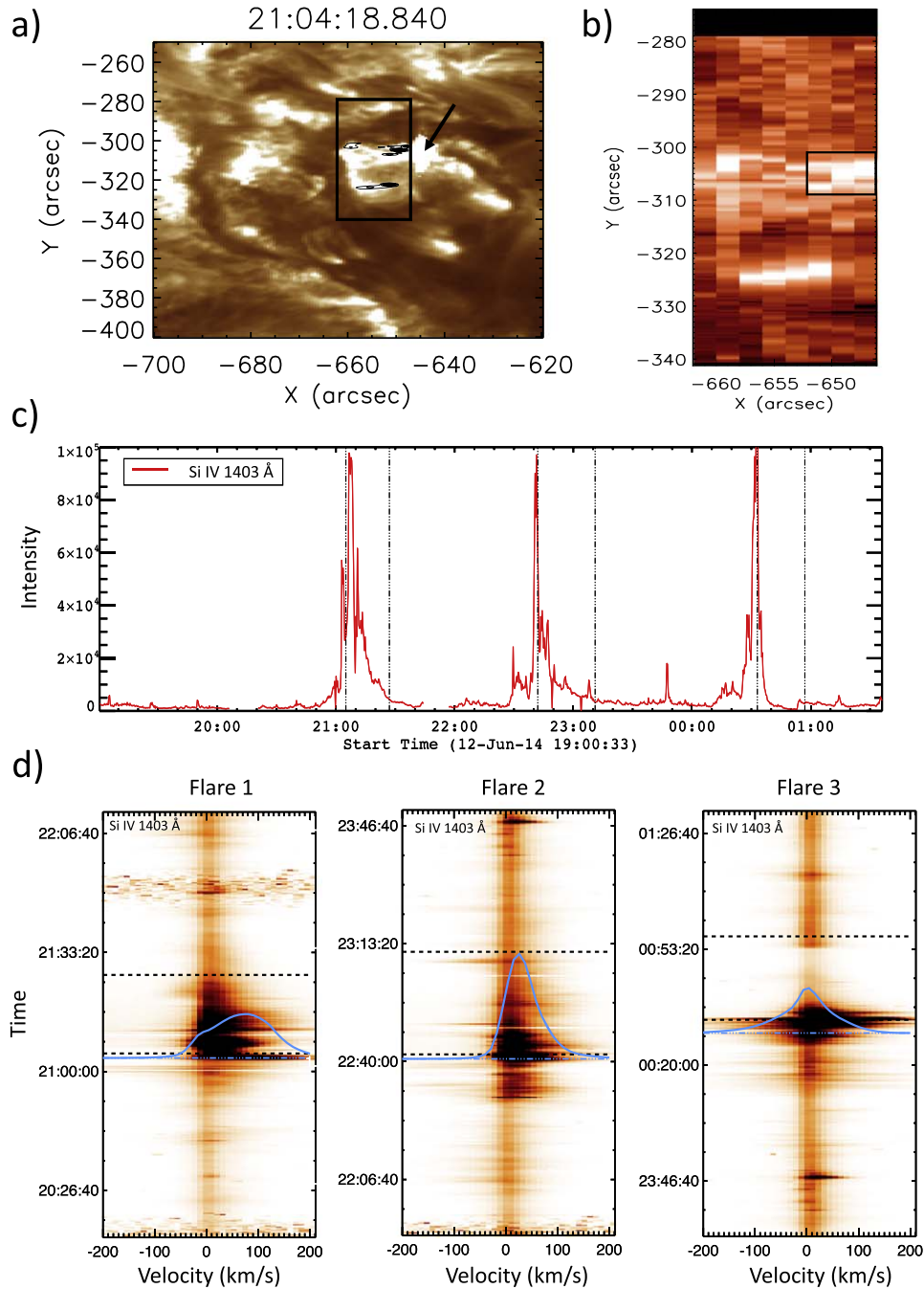


**Figure 6.** Panel (a) shows the *IRIS* Si IV 1403 Å raster field of view (black box) and *IRIS* intensity contours overlaid on AIA 193 Å. The black arrow marks the location of a recurrent bright point seen prior to and during the series of flares. Panel (b) shows the full *IRIS* Si IV 1403 Å raster intensity map at 21:04 UT. The overlaid box highlights the eastward edge of the recurrent bright point region. Panel (c) is the *IRIS* Si IV 1403 Å raster intensity lightcurve calculated within the box parked in panel (b). The dotted–dashed lines correspond to the flare start/end times as defined from AIA 94 Å data. Panel (d) shows the evolution of the *IRIS* Si IV 1403 Å line width, summed over the box shown in panel (b), with time on a velocity scale. Each profile corresponds to a 2 hr period around the peak of each flare in the sequence. The horizontal black dashed lines mark the start and end times of each flare. For each flare we also overplot a representative pre-flare spectra in blue.

parameter decay index is defined as:

$$n = -\frac{\partial \ln B}{\partial \ln R} \quad (7)$$

where  $B$  is the magnetic field strength and  $R$  is the radius of the torus, which is equivalent to height above the photosphere. In a region where  $n \geq 1.5$  the flux rope will be susceptible to torus instability (Kliem & Török 2006). Figure 11 shows the decay index profiles for each of the

four extrapolations. Decay index in these figures is plotted on a scale of 1.3–1.5, and is shown for an east–west orientated plane passing through the center of AR 12087. We can see that temporally, there is very little evolution in the decay index profiles. The plotted magnetic structures are located within a region where decay index is well below the  $\geq 1.5$  limit for the torus instability. Although decay index is only plotted in one east–west orientated plane, this behavior is also

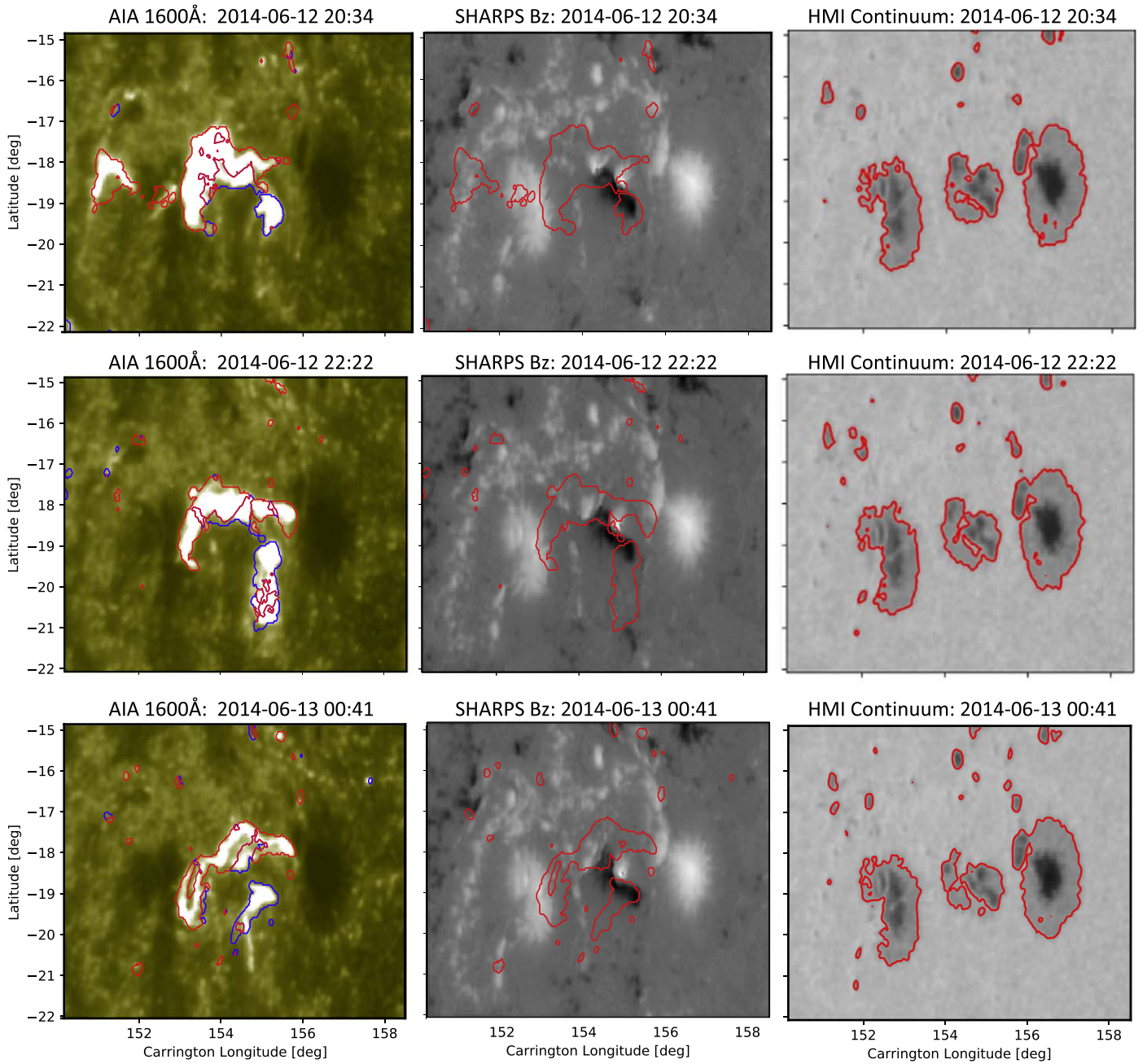


**Figure 7.** For flares 1, 2, and 3 (rows (a), (b), and (c), respectively), the first column shows AIA 1600 Å images with the total ribbon maps overlaid. Regions bound by red contours represent the ribbons that exist in positive polarity, while blue contoured regions represent ribbons within negative polarity. The second column shows the full total ribbon area overlaid onto the SHARPS  $B_z$  magnetogram image. The final column shows the HMI continuum images with the red contours highlighting the sunspot regions.

**Table 1**

$S_{\text{ribbon}}/S_{\text{spot}}$  for Each of the Flares in the Sequence

	$S_{\text{ribbon}}$	$S_{\text{spot}}$	$S_{\text{ribbon}}/S_{\text{spot}}$
Flare 1 (NE)	820.87	1486.75	0.55
Flare 2 (NE)	695.03	1534.85	0.45
Flare 3 (E)	585.95	1508.85	0.38

**Note.** All values are quoted in MSH (millionths of a solar hemisphere).

observed when this plane is moved northwards or southwards e.g., the observed magnetic structures are always found to be in a region stable to the decay index.

From our observations of AR 12087 and subsequent magnetic field modeling we have determined several insights about the sequence of flares under study. From our observational analysis we have seen that prior to flares 1 and 2 in the sequence flux cancellation was observed in a region close to the polarity inversion line in the center of AR 12087. Within this central portion of the AR 12087 there is a recurring bright region seen in both AIA and *IRIS* observations. From the *IRIS* observations of this region the bright region is seen to show intensity enhancements  $\sim 20$  minutes prior to flares 2 and 3. The ratio of flare ribbon area and sunspot area,  $S_{\text{ribbon}}/S_{\text{spot}}$ , for each flare were calculated and were found to be consistent with values found by Toriumi et al. (2017) for their respective

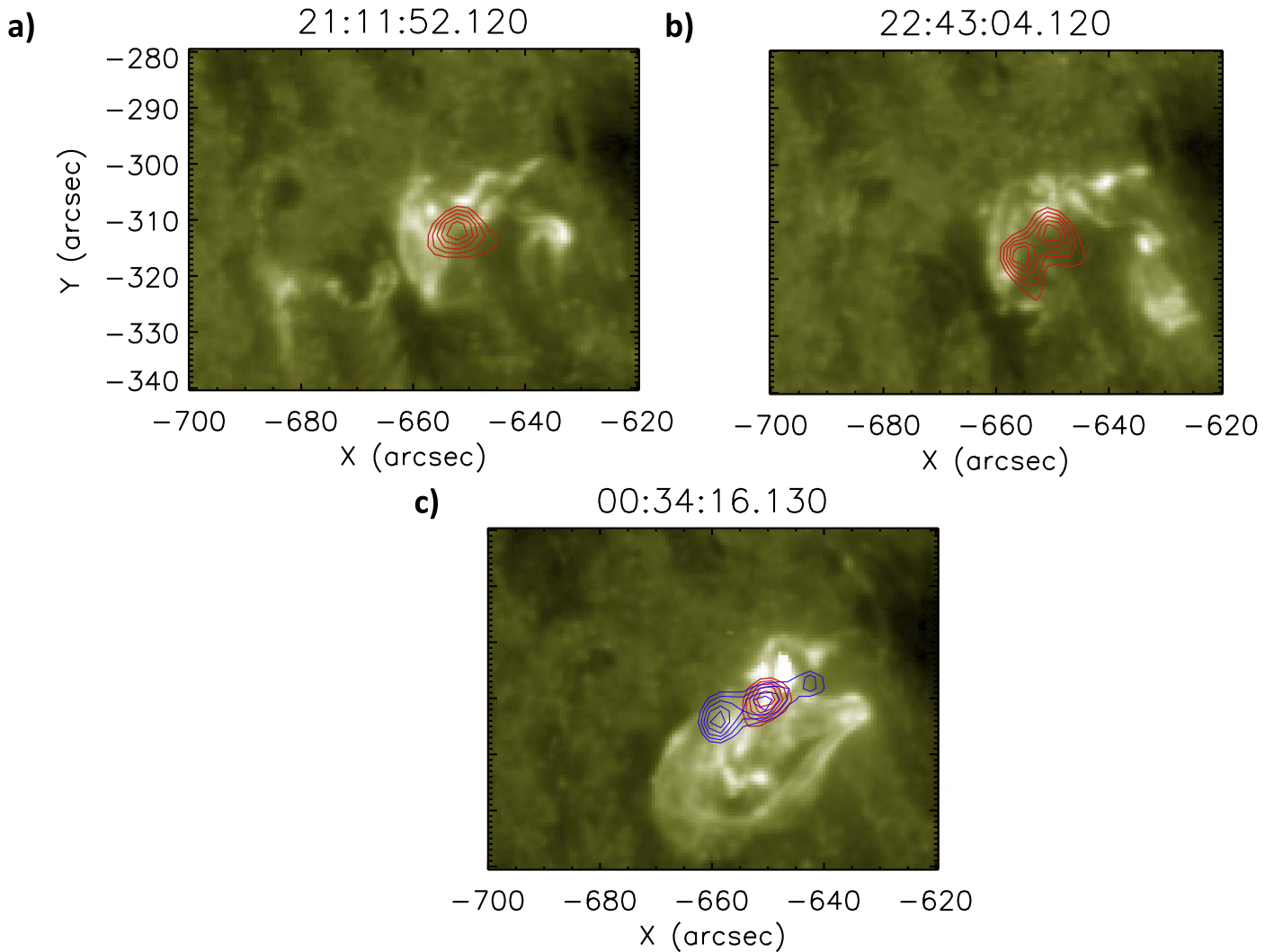


**Figure 8.** Rhesi contours overlaid onto AIA 1600 Å images. Red contours show emission in the 12–25 keV range, while blue contours show emission in the higher energy 25–50 keV range. The contours are plotted at 60, 70, 80, and 90%. Panel (a) shows the M1 flare at 21:11 UT, where we observe one unresolved low energy source; panel (b) shows the c-flare at 22:43 UT, where we observe two resolved sources in the low energy band; panel (c) shows the C 8 flare and eruption at +1 00:34 UT. Here we observe one unresolved low energy source and one resolved source in the higher energy band.

eruptive class. The series of NLFFF extrapolations resulted in the production of a twisted flux rope, which can be seen in Figure 9 and appears to reproduce the magnetic structure of AR 12087. Studying the quantities that can be calculated from the extrapolations, it was found that there were no significant changes in twist between the flares, and that the flux rope produced lay well within a region stable to the torus instability.

#### 4. Discussion

In the preceding section we have detailed the sequence of events leading to the eruption observed with the C 8 flare. Additionally we have investigated the pre-flare periods of all 3 flares to determine the presence of any possible observational differences between the otherwise morphologically similar flares that may provide evidence as to what triggered the eruption in the final flare.

Woods et al. (2017) investigated the hours prior to an X 1 flare, utilizing spectral observations from the *IRIS* spacecraft. This work identified blueshifted emission in the vicinity of a filament within the active region up to 40 minutes prior to the X 1 flare. These plasma flows showed blueshifts of up to

$200 \text{ km s}^{-1}$ . These spectral features were linked to possible tether-cutting reconnection occurring around the filament, possibly leading to the onset of flaring.

While pre-flare activity is observed before flares 1, 2, and 3, as both intensity enhancements and Doppler shifts, in the case of AR 12087 we see that the timescale for these intensity enhancements is far closer to flare onset than was seen in Woods et al. (2017). We see the first intensity enhancement observed by *IRIS* occurring  $\sim 20$  minutes before the onset of flares 2 and 3. Additionally, Woods et al. (2017)’s observations highlighted intermittent strongly blueshifted ( $-200 \text{ km s}^{-1}$ ) emission during this pre-flare activity. We can see from Figure 6 that the pre-flare spectra for flares 1, 2, and 3 do not show the intermittent behavior seen in earlier work, as well as not exhibiting the strongly blueshifted emission. Indeed this region shows emission that is redshifted, and does not reach equivalent velocities (peak  $\sim +100 \text{ km s}^{-1}$ ). The differences between these two sets of data suggests that the underlying cause of the pre-flare activity seen in both cases could be different. It is important to note however that while Woods et al. (2017)’s *IRIS* observations covered the majority of the region in which the flux rope was determined to

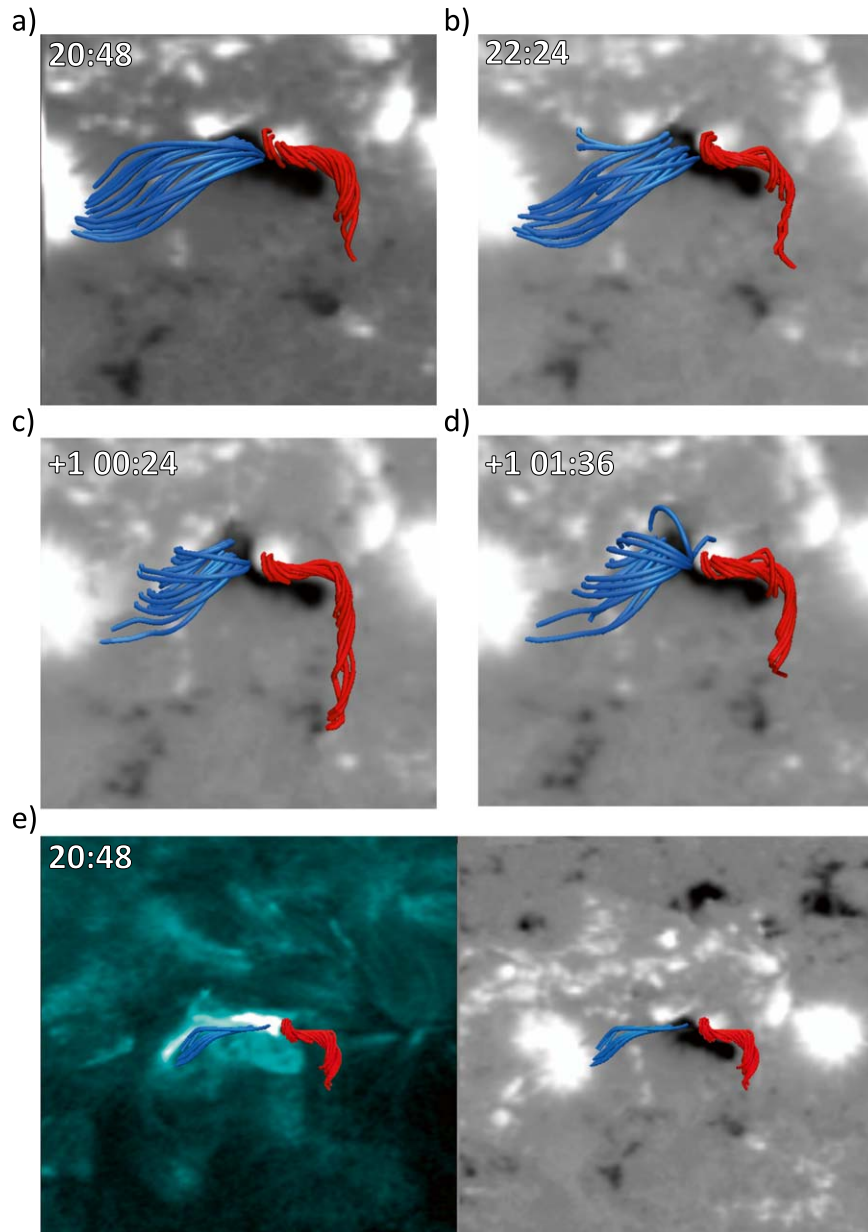


**Figure 9.** Results of the NLFFF extrapolations. The red field lines are plotted from a region of high twist in the central portion of the active region, the area of which is highlighted by the red box in panel (e). The blue field lines are plotted from a region to the east of the red field lines, shown by the blue box in panel (e). The field lines are overplotted onto the HMI SHARPS magnetic field data from which the NLFFF is extrapolated. Panels (a)–(d) chart the evolution in time at 20:48 UT, 22:24 UT, +1 00:24 UT, and +1 01:36 UT, respectively. Panel (e) shows a comparison of the extrapolated field lines to hot loops as observed in the AIA 131 Å channel.

be, in the case of AR 12087 the *IRIS* raster does not fully encompass the location of the flux rope as determined from the NLFFF extrapolations. In this case the *IRIS* raster does cover the edge of the recurring bright region. This could be seen to be analogous with a similar bright point discussed in Woods et al. (2017, 2018). This bright point (denoted region c) in the previous studies, did exhibit the fast intermittent blueshifts, unlike the region we study in this case, again building evidence that the pre-flare activity may be being driven by a different process.

While it seems unlikely that the pre-flare intensity enhancements we observe are related to the scenario presented in Woods et al. (2017), they are seen to occur in an area of the active region where similar flux cancellation was observed. From the HMI evolution in the central portion of the active

region (Figure 5), we observed clear evidence of flux cancellation prior to and during both flares 1 and 2. As we noted, evidence of cancellation is not clear before the eruptive C 8 flare. This cancellation is seen to begin  $\sim 20$  minutes prior to flares 1 and 2. Flux cancellation has been linked to the formation of magnetic flux ropes (van Ballegoijen & Martens 1989) that later erupt. The intensity enhancements could be an additional indicator that the magnetic field within the central portion of the active region is being reorganized by, for example, flux cancellation. This flux cancellation could then allow the build up of helical field lines within the flux rope, which would likely lead to an increase in the twist measured in the flux rope. This increasing twist could in theory lead to the destabilization, via kink instability, of the flux rope and its subsequent eruption. This scenario was suggested by

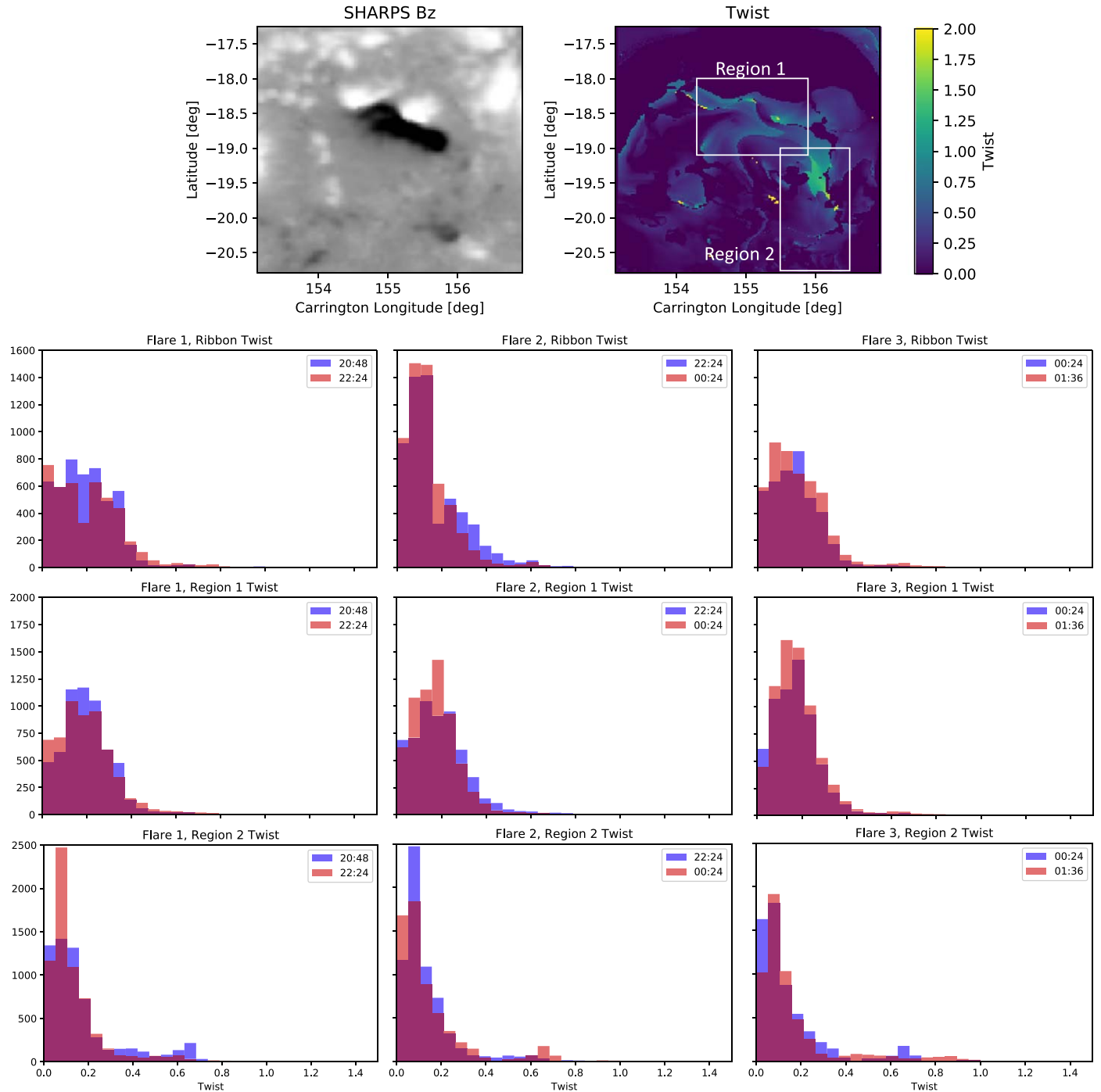


**Figure 10.** In panel (a), the left hand image shows the HMI SHARPS  $B_z$  component of photospheric magnetic field from which the extrapolations and subsequently twist were calculated for context. The right hand panel shows the twist map, with two areas, regions 1 and 2 are marked by the overplotted boxes, in which the evolution of twist between NLFFF time steps was investigated. Panel (b) shows the evolution of twist in region one before and after each flare. Likewise, panel (c) shows the same evolution for region 2.

Kumar et al. (2015) as a possible result of the flux cancellation that we have also observed in this active region.

Our NLFFF extrapolations allow this hypothesis to be tested, as twist is one of the properties that can be determined from the extrapolations. Figure 10 showed twist distributions before and after each of the flares for the same region in which we measured the evolution of magnetic flux. Twist does not in fact increase by a meaningful amount or reach the level ( $T_w \geq 1.5$ ) at which it would make a flux rope susceptible to kink

instability based on the results of our modeling. A further observational test of this conjecture would be through observation of untwisting the kinking of the flux rope in the spectroscopic observations, e.g., Williams et al. (2009). However, the *IRIS* spectrometer’s field of view, shown in Figure 6(a), does not cover the region in which the extrapolation tells us the flux rope lies. This is unfortunate as it means we cannot definitively prove the kinking is not observed. However, from what information we do have it is

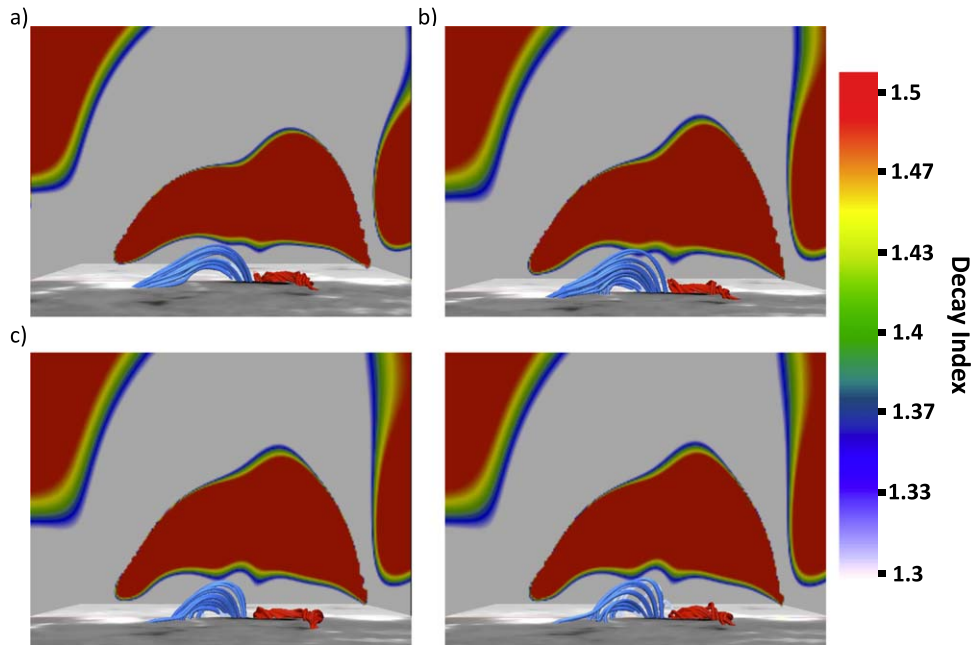


**Figure 11.** Panels (a)–(d) show the evolution of decay index and its relation to the field lines shown in Figure 9. The decay index in these figures is shown on an east–west orientated plane that passes through the central region of AR 12087.

highly suggestive that another mechanism must be responsible for the destabilization of the flux rope and ensuing eruption.

Woods et al. (2018) used the same extrapolation method used in this work to investigate the filament eruption associated with the 2014 March 29 X1 flare. In this work the authors identified that tether-cutting reconnection occurring at a region of flux cancellation between a flux rope and a nearby loop system could result in the destabilization of the flux rope subsequently leading to its eruption. We notice similarities in the morphology of the extrapolation results in the Woods et al. (2018) case and those resulting from the extrapolations presented in Section 3.2, where we see the twisted red field lines meeting a loop system (blue field lines) that extends westwards. At this point of intersection is the recurrent pre-flare bright region that is observed in the AIA and *IRIS* data, which again is similar to what was observed by Woods et al. (2018). In the Woods et al. (2018) case however, the eruptive flux rope lay in very close proximity to a region where the decay index was greater than the threshold necessary to allow torus instability to occur. From Figure 11 we have seen that in the case of AR 12087 the flux rope that we have identified lies well below the region in which it would be susceptible to torus instability. The mechanism through which Woods et al. (2018) suggest the flux rope observed in that paper enters the torus unstable region is the DAI. Ishiguro & Kusano (2017) who first proposed DAI as a possible trigger of eruptions note that even in cases where a current loop, or flux rope, are in a region where decay index is insufficient to lead to the onset of torus instability, the DAI can still provide a driver for eruption. For this reason we cannot exclude the possibility that the DAI could lead to the onset of the eruption of the flux rope during the final flare.

As it seems that instabilities cannot be conclusively determined to be responsible for this eruption, consideration must then be given to the overlying field above the central active region and the flux rope therein. Figure 12 shows the 22:24 UT extrapolation where the red and blue field lines are

the same as those described in Figure 3.2. The purple field lines show the overlying magnetic field. This overlying field is comprised predominantly of two loop structures each linking a region of positive field to the predominantly negative field on the central portion of the active region. This can be clearly seen in panel (a) of Figure 12, which shows the field as viewed from the south. Panel (b) shows a side on view of the same magnetic field lines. We can see that above the main looped field lines there are several field lines that extend out of the extrapolation box. To the north these open field lines extend vertically, while to the south the overlying field lines are inclined strongly. The topology of these magnetic field lines is very similar to that of the fan-spine topology, where the field lines extending out of the extrapolation box to the south form the spine. While it would require an additional NLFFF extrapolation with a larger field of view to determine, it is highly likely that these spine field lines connect to the LR region that we discussed earlier and was shown in Figure 4. Kumar et al. (2015) also reached the conclusion that the overlying field may exhibit fan-spine topology, as they note that the appearance of the quasi-circular ribbons is indicative of this topology (e.g., Masson et al. 2009). The results of our NLFFF extrapolation support their conclusion. The identification of the fan-spine topology could present a possible explanation for the trigger of the eruption during flare 3. The magnetic breakout model of Antiochos et al. (1999) presents a scenario in which overlying unsheared magnetic field above sheared flux is weakened by reconnection allowing eruptions to proceed. Aulanier et al. (2000) linked breakout reconnection to the fan-spine topology where the reconnection occurs at a null point in the corona, at the intersection of the fan-like field lines, and the spine that extends away from it. This has been observationally seen by authors, such as Fletcher et al. (2001) and Li et al. (2018). In panel (c) of Figure 12 we see that at the intersection of the fan-like field line and the spine in our extrapolation we see larger values of  $|J|/|B|$ . This is suggestive of this being the

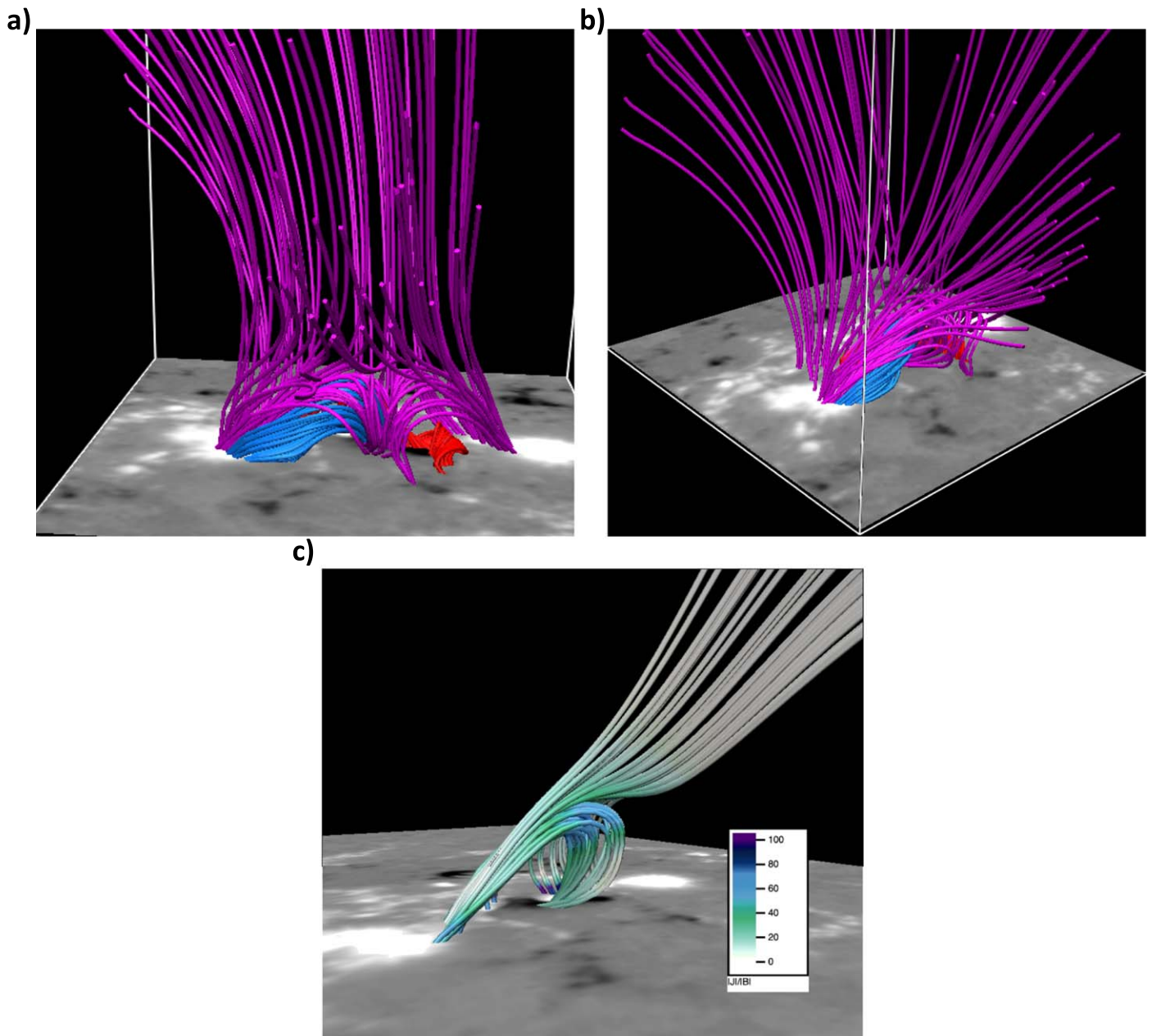


**Figure 12.** Panels (a) and (b) show the overlying magnetic field (purple) above the twisted field lines explored in Figure 3.2, seen to exhibit a fan-spine topology. Panel (c) shows  $|J|/|B|$  values overlaid on the fan-spine field lines.

location of a null point at which breakout reconnection could occur. As noted earlier if the spine structure were to be linked to the region we denoted LR, the intensity enhancements that we see in the lightcurve for this region (Figure 4(c)) prior to and during flares 1 and 2 could be due to heating from particle acceleration caused by this breakout reconnection occurring at the null point of the fan-spine structure. Weakening of the overlying magnetic field during flares 1 and 2 through breakout reconnection could allow the observed eruption to proceed during flare 3. Additionally, as we noted in our discussion of Figure 4, the presence of another active region (AR 12092) in close proximity to AR 12087, which exhibits a failed eruption at the same time as the eruption we are studying, could further destabilize the overlying magnetic fields above AR 12087 allowing the eruption to proceed.

## 5. Conclusions

In this paper, observations and NLFFF extrapolations of a series of three flares have been presented. Examining the results of our observations in the context of existing studies of pre-flare activity. While we do see pre-flare intensity enhancements and evidence of flux cancellation within AR 12087 it seems unlikely that this is the result of the scenario of flare and eruption triggering presented in Woods et al. (2017, 2018). Our NLFFF extrapolations have confirmed the conclusion of Kumar et al. (2015) of the presence of a fan-spine topology in the overlying magnetic field. Despite strong similarities between the structure of the core field lines in the extrapolations to those analyzed in Woods et al. (2018), it seems highly unlikely that the scenario presented therein for eruption triggering is occurring in this case due the flux rope identified in this AR

being situated far from a region where decay index would make it susceptible to the torus instability. Additionally, from the analysis of the evolution of twist within the extrapolations it is concluded that the eruption is unlikely to have been driven by kink instability. The fan-spine topology does raise the possibility that the overlying magnetic field was weakened by breakout reconnection during flares 1 and 2. This decrease in the overlying magnetic field could then have resulted in the eruption during flare 3 due to the weaker magnetic field constraining the flux rope.

The sequence of flares described in this work shows just how complex flare and eruption triggering is, e.g., superficially the three flares are morphologically similar but show different eruptive outcomes. Also, when compared to other events such as in Woods et al. (2018), we again find similar but very different results. This makes it clear that while there have been many advances in the studies of flare and eruption triggering in recent years, each event is in many ways unique and highly complex.

The authors would like to thank KD Leka and Sung-Hong Park for their helpful discussions during the preparation of this work. *IRIS* is a NASA Small Explorer mission developed and operated by LMSAL with mission operations executed at NASA Ames Research center and major contributions to downlink communications funded by ESA and the Norwegian Space Centre. HMI and AIA are instruments on board *SDO*, a mission for NASA's Living with a Star program. Data are provided courtesy of the *SDO* science team. NLFFF extrapolations were visualized using VAPOR (Clyne & Rast 2005; Clyne et al. 2007), which is a product of the National Centre for Atmospheric Research's Computational and Information Systems Lab. The authors would also like to thank NASA for their support of the *RHESSI* mission. L.K.H. and S.A.M. acknowledge STFC consolidated grant ST/N000722/1 for their funding.

*Facilities:* *IRIS*, *SDO*, *RHESSI*.

*Software:* Sunpy.

#### ORCID iDs

Magnus M. Woods  <https://orcid.org/0000-0003-1593-4837>

Satoshi Inoue  <https://orcid.org/0000-0001-5121-5122>

Louise K. Harra  <https://orcid.org/0000-0001-9457-6200>

Sarah A. Matthews  <https://orcid.org/0000-0001-9346-8179>

Kanya Kusano  <https://orcid.org/0000-0002-6814-6810>

#### References

- Antiochos, S. K., DeVore, C. R., & Klimchuk, J. A. 1999, *ApJ*, **510**, 485
- Aulanier, G., DeLuca, E. E., Antiochos, S. K., McMullen, R. A., & Golub, L. 2000, *ApJ*, **540**, 1126
- Bateman, G. 1978, *MHD Instabilities* (Cambridge, MA: MIT Press)
- Bobra, M. G., Sun, X., Hoeksema, J. T., et al. 2014, *SoPh*, **289**, 3549
- Clyne, J., Mininni, P., Norton, A., & Rast, M. 2007, *NJPh*, **9**, 301
- Clyne, J., & Rast, M. 2005, *Proc. SPIE*, **5669**, 284
- Dedner, A., Kemm, F., Kröner, D., et al. 2002, *JCoPh*, **175**, 645
- DePontieu, B., Title, A. M., Lemen, J. R., et al. 2014, *SoPh*, **289**, 2733
- Fletcher, L., Metcalf, T. R., Alexander, D., Brown, D. S., & Ryder, L. A. 2001, *ApJ*, **554**, 451
- Harra, L. K., Schrijver, C. J., Janvier, M., et al. 2016, *SoPh*, **291**, 1761
- Inoue, S. 2016, *PEPS*, **3**, 19
- Inoue, S., Magara, T., Pandey, V. S., et al. 2014, *ApJ*, **780**, 101
- Ishiguro, N., & Kusano, K. 2017, *ApJ*, **843**, 101
- Kliem, B., & Török, T. 2006, *PhRvL*, **96**, 255002
- Kumar, P., Yurchyshyn, V., Wang, H., & Cho, K.-S. 2015, *ApJ*, **809**, 83
- Lemen, J. R., Title, A. M., Akin, D. J., et al. 2012, *SoPh*, **275**, 17
- Li, T., Yang, S., Zhang, Q., Hou, Y., & Zhang, J. 2018, *ApJ*, **859**, 122
- Lin, R. P., Dennis, B. R., Hurford, G. J., et al. 2002, *SoPh*, **210**, 3
- Masson, S., Pariat, E., Aulanier, G., & Schrijver, C. J. 2009, *ApJ*, **700**, 559
- Moore, R. L., & Labonte, B. J. 1980, in *IAU Symp. 91, Solar and Interplanetary Dynamics*, ed. M. Dryer & E. Tandberg-Hanssen (Dordrecht: Reidel), 207
- Moore, R. L., Sterling, A. C., Hudson, H. S., & Lemen, J. R. 2001, *ApJ*, **552**, 833
- Nitta, N. V., & Hudson, H. S. 2001, *GeoRL*, **28**, 3801
- Pesnell, W. D., Thompson, B. J., & Chamberlin, P. C. 2012, *SoPh*, **275**, 3
- Polito, V., Del Zanna, G., Valori, G., et al. 2017, *A&A*, **601**, A39
- Romano, P., Zuccarello, F., Guglielmino, S. L., et al. 2015, *A&A*, **582**, A55
- Sadykov, V. M., Kosovichev, A. G., Sharykin, I. N., Zimovets, I. V., & Vargas Dominguez, S. 2016, *ApJ*, **828**, 4
- Sakurai, T. 1982, *SoPh*, **76**, 301
- Scherrer, P. H., Schou, J., Bush, R. I., et al. 2012, *SoPh*, **275**, 207
- Sharykin, I. N., Sadykov, V. M., Kosovichev, A. G., Vargas-Dominguez, S., & Zimovets, I. V. 2017, *ApJ*, **840**, 84
- Temmer, M., Veronig, A. M., Kontar, E. P., Krucker, S., & Vršnak, B. 2010, *ApJ*, **712**, 1410
- Toriumi, S., Schrijver, C. J., Harra, L. K., Hudson, H., & Nagashima, K. 2017, *ApJ*, **834**, 56
- Török, T., & Kliem, B. 2005, *ApJL*, **630**, L97
- van Ballegoijen, A. A., & Martens, P. C. H. 1989, *ApJ*, **343**, 971
- Vršnak, B. 2008, *AnGeo*, **26**, 3089
- Williams, D. R., Harra, L. K., Brooks, D. H., Imada, S., & Hansteen, V. H. 2009, *PASJ*, **61**, 493
- Woods, M. M., Harra, L. K., Matthews, S. A., et al. 2017, *SoPh*, **292**, 38
- Woods, M. M., Inoue, S., Harra, L. K., et al. 2018, *ApJ*, **860**, 163